Chemical Engineering Journal 490 (2024) 151578

Contents lists available at ScienceDirect

Chemical Engineering Journal

journal homepage: www.elsevier.com/locate/cej

Liquid Na-K alloy is not viable anode material for High-Performance Na-Ion batteries

Hyeongjun Koh [a], Mohamed H. Hassan [a], Stella Lin [a], Lin Wang [a], Eric A. Stach [a,b,*], Eric Detsi [a,*]

[a] Department of Materials Science & Engineering, University of Pennsylvania, Philadelphia, PA 19104, USA
[b] Laboratory for Research on the Structure of Matter, University of Pennsylvania, Philadelphia, PA 19104, USA

ARTICLE INFO

Keywords:
Na-ion batteries
Liquid sodium–potassium metal anode
Plating/stripping
Dendrite formation
"self-healing" anode
Cryogenic focused ion beam scanning electron microscopy

ABSTRACT

Liquid sodium–potassium alloy Na_xK_{100-x} at. % (≈14 < x < 70 at room temperature) has been proposed as a dendrite-free liquid metal anode for Na-ion batteries. Nevertheless, controversy surrounds the use of Na_xK_{100-x} as a Na-ion battery anode due to the presence of the two competitive redox-active species, Na/Na^+ and K/K^+. To resolve this ongoing controversy, we use x-ray diffraction (XRD) and cryogenic-focused ion beam/scanning electron microscopy (cryo-FIB/SEM) to investigate liquid $Na_{50}K_{50}$ electrodes cycled in symmetric cells using Na-ion electrolytes. We find that the reaction overpotential abruptly increases after ≈ 40 cycles. Cryo-FIB/SEM reveals the precipitation of K salts, which confirms that K/K^+ species are redox-active in Na-ion electrolytes. Such an effect progressively leads to irreversible leaching of K from the initial liquid $Na_{50}K_{50}$ composition, resulting in a loss of liquid metal properties. Consequently, our results suggest that Na_xK_{100-x} cannot sustainably function as a liquid metal anode in Na-ion batteries.

1. Introduction

Liquid sodium–potassium alloy (Na_xK_{100-x} at. % where ≈14 < x < 70 at room temperature, as shown in the phase diagram in Scheme 1a) has emerged as a promising metal anode candidate for Na-ion batteries [1–4]. The fact that Na_xK_{100-x} is liquid at room temperature offers potential advantages such as "self-healing" capabilities to enhance battery cyclability and recovery from structural deformation [4–7]. This can be true even during high-power operations due to fast kinetics in the liquid state [8–10]. Since Goodenough and colleagues [1] first demonstrated the feasibility of liquid Na_xK_{100-x} at. % (x ≈ 46) as a Na-ion battery anode, extensive research efforts have been devoted to the development of Na_xK_{100-x} anodes, both with liquid electrolytes [11–14] and as components in solid-state electrolyte systems [15–19]. Because some Na-ion cathode materials exhibit good cyclability and acceptable gravimetric capacity [20–22], coupling these cathodes with Na_xK_{100-x} anode could enable high-performance full-cell Na-ion batteries.

While Na_xK_{100-x} liquid anode offers various advantages, the presence of two redox-active elements (i.e., two working ions) with nearly similar value of standard reduction potentials raises concerns about potential asymmetric reactions during battery cell charging and discharging. To evaluate their redox behavior, we computed the standard reduction potentials of Na and K in liquid $Na_{50}K_{50}$, as depicted in Scheme 1b. This was determined by calculating the Gibbs free energy of the liquid phase at room temperature (25 °C) and the chemical potentials of each element at the composition ratio (details provided in the Supplementary materials and Figure S1 [23,24]). The analysis indicates that K in the alloy exhibits higher reactivity than Na, given that the chemical potential of K is lower than that of Na. The calculation further suggests that the higher reactivity of K extends beyond $Na_{50}K_{50}$ to any liquid phase in the range of Na_xK_{100-x}, where 14 < x < 70 (Figure S2). This reactivity difference could induce an asymmetric redox reaction in full battery cells, as displayed in Scheme 1c. For example, during charging, the anode – in this case $Na_{50}K_{50}$ electrode – will plate Na from the Na-ion electrolyte while the Na cathode will release sodium ions into the liquid electrolyte. Since thermodynamics predicts that the most reactive element must be oxidized first during discharge, K from $Na_{50}K_{50}$ will be stripped and dissolved into the electrolyte, leading to the asymmetric redox reaction. This raises a critical question: will Na_xK_{100-x} anode be suitable for Na-ion batteries?

The question concerning the viability of Na_xK_{100-x} anode sparked an intriguing controversy in the literature in recent years. Previous research found that some K can dissolve into the electrolyte during the redox reaction. Those studies suggested that the Na_xK_{100-x} anodes could

* Corresponding authors.
E-mail addresses: stach@seas.upenn.edu (E.A. Stach), detsi@seas.upenn.edu (E. Detsi).

https://doi.org/10.1016/j.cej.2024.151578
Received 20 February 2024; Received in revised form 12 April 2024; Accepted 22 April 2024
Available online 23 April 2024

accommodate both Na and K ions, and the primary ionic carrier could be determined by the choice of cathode [25,26]. On the other hand, other studies suggested that Na_xK_{100-x} may not be practical in Na-ion electrolytes due to the preferential dissolution of K [26,27]. As such, it is critical to understand the feasibility of Na_xK_{100-x} as self-healing liquid anodes for developing high-performance Na-ion batteries.

2. Results and discussion

In order to determine the feasibility of using liquid $Na_{50}K_{50}$ as an anode in Na-ion batteries, we prepared liquid $Na_{50}K_{50}$ electrodes by infiltrating the alloy into a three-dimensional (3D) carbon paper matrix (6 mm in diameter). The use of a 3D carbon paper matrix is necessary to confine the liquid $Na_{50}K_{50}$. Because of the poor wettability of $Na_{50}K_{50}$, the carbon papers were pre-heated to 400 °C for 5 min in an inert environment (argon-filled glovebox) which facilitates the formation of carbon-potassium compounds (KC_8) [14]. Typically, KC_8 spontaneously forms upon contact with the liquid metal after the pre-heating step, and $Na_{50}K_{50}$ spontaneously fills the space covering the carbon matrix (Fig. 1a).

To visualize the distribution of $Na_{50}K_{50}$ within the 3D carbon matrix, we used a cryogenic Xe^+ plasma focused ion beam/scanning electron microscope (cryo-FIB/SEM) to cut through the $Na_{50}K_{50}$ carbon paper. (Fig. 1b). Ion milling liquid metal at room temperature is challenging due to its high surface tension and fluidic nature [10,28,29]. We used cryogenic ion beam milling to make cross-sections of the electrode. Fig. 1b shows the entire ≈150 μm-thick cross-section of a $Na_{50}K_{50}$ alloy/carbon paper electrode after ion beam milling. The bright contrast and the dark contrast indicate the presence of liquid metal and carbon fibers, respectively. To analyze the composition by energy dispersive spectrum (EDS), a small cross-section was cut out (Fig. 1c). The EDS map of the boxed region in Fig. 1c revealed that Na and K are present in the liquid electrode (Fig. 1d). The cross-sectional image of the liquid metal electrode suggests that $Na_{50}K_{50}$ successfully infiltrated into the carbon paper without forming any voids.

The contrast difference in secondary electron imaging in Fig. 1c indicates the presence of Na-rich and K-rich regions, shown in the EDS maps (Fig. 1d), which could be attributed to composition or phase segregation during cryogenic quenching. The composition ratio of different regions was calculated by determining the integrated intensity of Na and K from the EDS spectrum (Fig. 1e). The Na-to-K atomic ratio in the region marked as #1 with a dark contrast is 52:48, corresponding to only to 2 % deviation from the nominal ratio of 50:50, while the region marked as #2 with a bright contrast shows a percentage ratio of 28:72, corresponding to 22 % deviation from the nominal ratio of 50:50. As suggested above, we believe such local concentration differences arise during quenching of the electrode in liquid nitrogen. Indeed, the fast-cooling procedure could give rise to a coring effect, which is commonly seen during quenching of liquid alloys in metallurgy [30]. Despite the local variations in the chemical composition caused by cryo-quenching, the overall Na-to-K atomic percentage ratio from the entire EDS map in Fig. 1d was 43:57, which is close to the desired nominal composition of 50:50, within 7 % deviation. Apart from the composition analysis, the XRD measurement suggests that there is no crystalline diffraction, except for KC_8. This is consistent with the $Na_{50}K_{50}$ being a liquid metal, in that there is evidence of order that would lead to diffraction peaks (Fig. 1f).

The electrochemical performance of liquid $Na_{50}K_{50}$ confined in carbon papers was investigated by using a symmetric cell configuration ($Na_{50}K_{50}$ | Na-ion electrolyte | $Na_{50}K_{50}$) assembled using CR 2032 coin cells and cycled in the voltage window between −0.9 V and + 0.9 V vs. Na/Na^+ at a constant current density of ± 0.4 mA/cm^2 to a capacity of 1 mAh/cm^2. The mass loading of $Na_{50}K_{50}$ was about 2.8 mg in the carbon papers (6 mm diameter). We initially used 1 M $NaClO_4$ in a mixture of ethylene carbonate (EC)/dimethyl carbonate (DMC) (1:1 v/v) with 5 % volume fraction of fluoroethylene carbonate (FEC) as the electrolyte. The red curve in Fig. 2a shows the typical voltage vs. time profile (first four cycles) obtained from the $Na_{50}K_{50}$ | $NaClO_4$-EC-DMC-FEC | $Na_{50}K_{50}$ symmetric cell, and the black curve represents the voltage vs. time profile obtained from a Na | $NaClO_4$-EC-DMC-FEC | Na symmetric cell used for control experiments. The voltage profile of the Na symmetric cell showed two distinct plateaus as indicated by the 2nd and 3rd arrows in Fig. 2a, along with an initial spike in voltage indicated by the 1st arrow. The initial voltage spike indicated by the 1st arrow is associated with the nucleation overpotential when Na ions in the liquid electrolytes are reduced to solid Na nuclei at the electrode surfaces. Once stable Na nuclei are formed, they grow along easy-growth directions to form dendritic structures. During this growth process, a lower voltage plateau is first observed when Na is stripped from the dendritic structures (e.g., mossy dendrites [31]) formed on the oxidizing electrode, followed by a higher voltage plateau when Na is removed from the bulk Na electrode instead of from Na dendrites on the oxidizing electrode [31]. On the other hand, although the voltage profile of the $Na_{50}K_{50}$ symmetric also showed a spike in voltage associated with the formation of solid nuclei from reduced Na ions onto the liquid electrode, we observed a uniform increase in the voltage profile instead of two distinct voltage plateaus as with the Na symmetric cell. This gradual increase in voltage implies that the reaction overpotentials increase during the growth process, which suggests the formation of heterogeneous solid structures on the liquid metal surface, as will be proven later.

The red curve in Fig. 2b indicates that the cycling life of the $Na_{50}K_{50}$ symmetric cell is unexpectedly poor, although the use of a liquid metal has been postulated to improve battery lifespan [1]. The cell experienced an abrupt increase in overpotential after 170 h of cycling (≈ 35 cycles), and the cycling did not last for more than ≈ 250 h (corresponding to ≈ 50 cycles), when the cell exhibited huge overpotentials. Such poor cycling performance was not apparent in the Na symmetric cell, which can cycle more than 700 h before it short-circuited, as

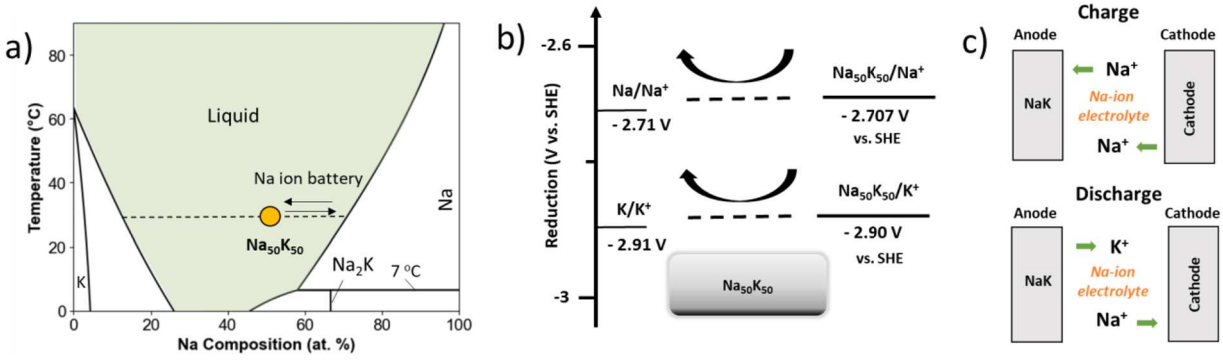

Scheme 1. Our hypothesis regarding asymmetric electrochemical reactions during charge and discharge. a) Equilibrium phase diagram of Na-K binary alloy. b) Standard reduction potentials of Na and K in $Na_{50}K_{50}$. c) An asymmetric redox reaction is caused by the lower reduction potential of K compared to Na.

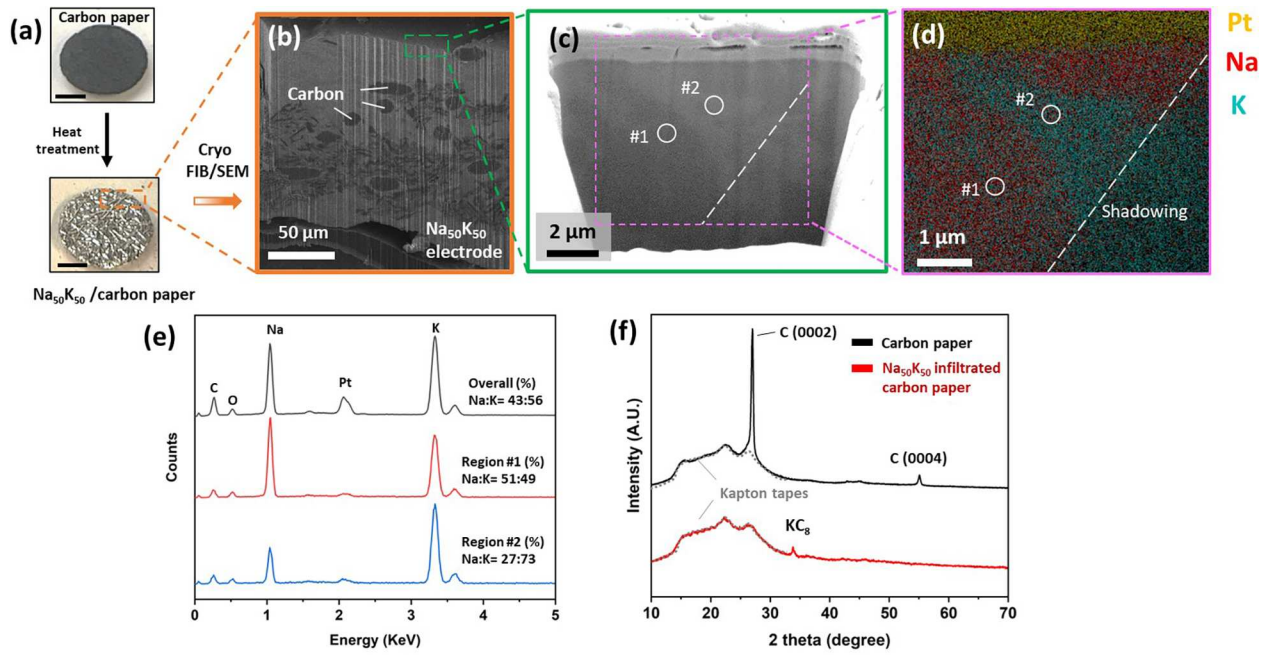

Fig. 1. Preparation of $Na_{50}K_{50}$ electrodes. (a) Images of the carbon paper before and after $Na_{50}K_{50}$ infiltration. Inset in (a) is 2 mm. (b) A cross-sectional SEM image of the entire electrode after cryo-milling. (c) A cross-sectional SEM image of the $Na_{50}K_{50}$ electrode close to the surface. The top surface of the electrode was coated with an organometallic Pt mask. (d) A cryo-EDS map from the boxed region in (c) showing Na and K distribution. The dashed line in (c) and (d) is where the shadowing effect is dominant because of the EDS detector position. Low-energy EDS signals from carbon, oxygen, and sodium were not detected efficiently in this region. (e) EDS elemental spectrum collected from regions #1, #2, and from the entire region in (d). When the overall composition was calculated, the area affected by the shadowing was not counted. (f) X-ray diffraction measurements before and after $Na_{50}K_{50}$ infiltration into the carbon papers.

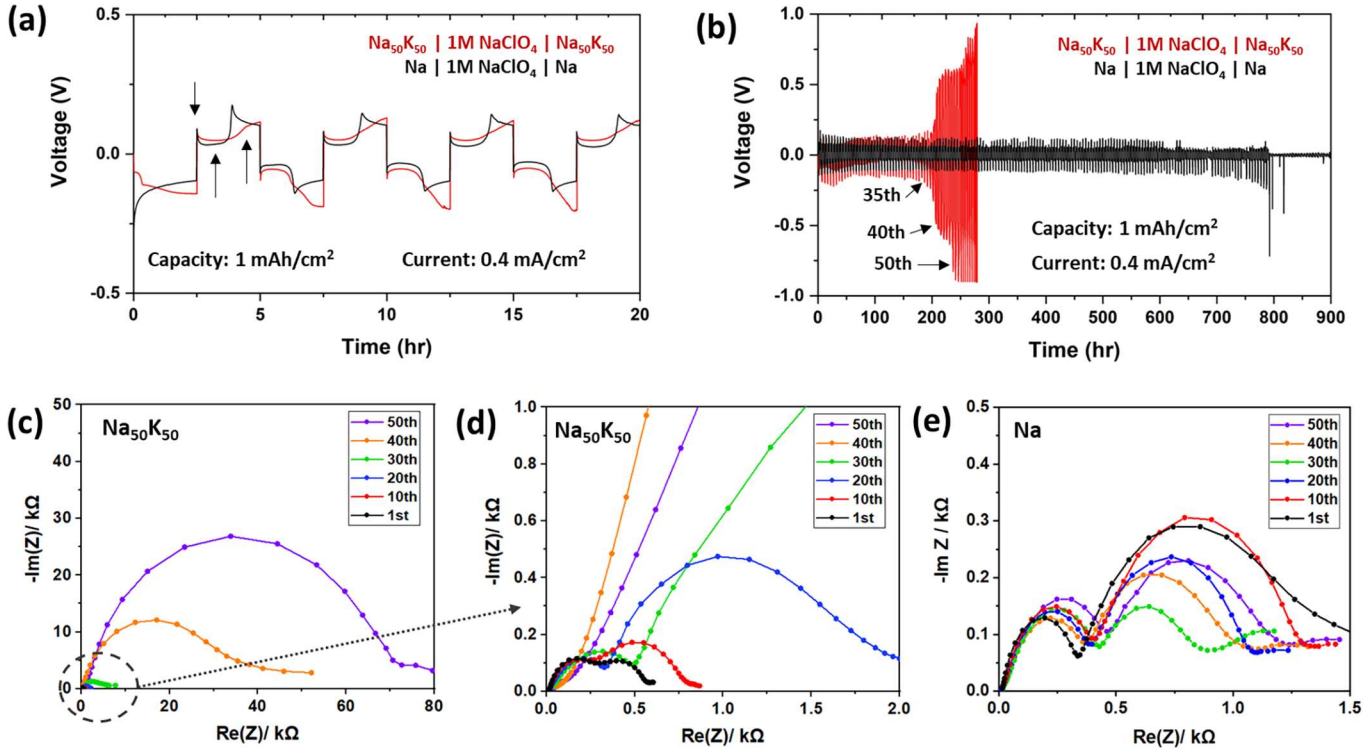

Fig. 2. Cycling performance of Na and $Na_{50}K_{50}$ symmetric cells. (a) Voltage profiles from the first 20 h of cycling of the two-symmetric cell at a current density of 0.4 mA/cm^2 to a capacity of 1 mAh/cm^2. (b) Cyclability between the Na and $Na_{50}K_{50}$ symmetry cell. EIS data of (c-d) the $Na_{50}K_{50}$ and (b) the Na symmetry cells cycled under the same condition as in (a) and (b).

illustrated by the black curve in Fig. 2b.

EIS measurements (Nyquest plots, Fig. 2c and d) show that the charge transfer resistance of the $Na_{50}K_{50}$ symmetric cell drastically increased during cycling. For example, the semi-circle diameter of 50th cycle (purple curve, Fig. 2c) is huge compared to that of the 30th and the 40th cycle (green and orange curve, Fig. 2c). Fig. 2d shows the same EIS

data at a higher magnification where two semi-circles can now be distinguished. These two semi-circles represent the resistance through solid electrolyte interphase (SEI) and the charge-transfer resistance, respectively [32]. These data suggest that after the 30th cycle, the charge-transfer resistance grew significantly. The total impedance of 50th cycle (≈ 70 kΩ) is ≈ 350 times that of the 1st cycle (≈ 0.5 kΩ). Unlike the $Na_{50}K_{50}$ cell, the EIS of the Na symmetry cell did not experience a drastic increase in SEI resistance or charge-transfer resistance throughout the cycling process (Fig. 2e). The huge increase in resistance in the $Na_{50}K_{50}$ symmetric cell implies the ion and electron transport have been significantly impeded, which leads to the high overpotentials in the $Na_{50}K_{50}$ symmetric cell.

To further investigate the unexpected failure of the liquid $Na_{50}K_{50}$ electrode, we examined this electrode after the 1st and 40th cycles using cryo-FIB/SEM (Figs. 3 and 4). Fig. 3a–f shows the top surface SEM image, and associated EDS elemental maps (Na, K, Cl, and C) of the electrode after the 1st cycle. In Fig. 3a, crystallites and needle-shaped Na dendrites were formed on the electrode surface. The EDS maps in Fig. 3d and e indicate the rich presence of K and Cl in these crystalline particles, and XRD measurements confirmed that they are $KClO_4$, as discussed

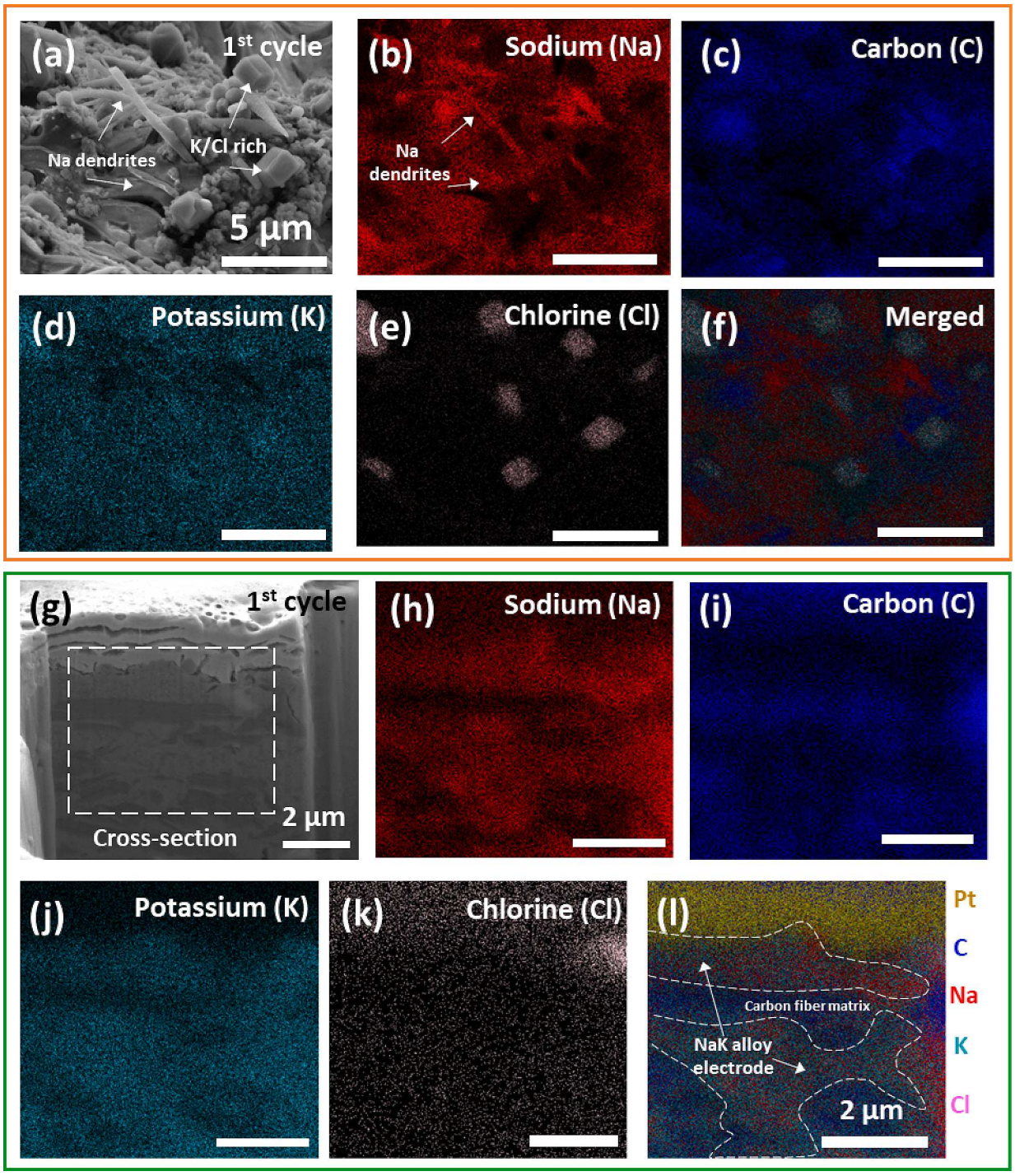

Fig. 3. Cryo-FIB/SEM images of the top surface and a cross-section after the first charge/discharge cycle from the $Na_{50}K_{50}$ electrode. (a) SEM image and (b-f) Cryo-EDS maps identified K and Cl rich particles and Na dendrites. (g-l) Cross-section milled by cryo-FIB milling and associated EDS maps show that the first cycle electrode remains rich in Na and K.

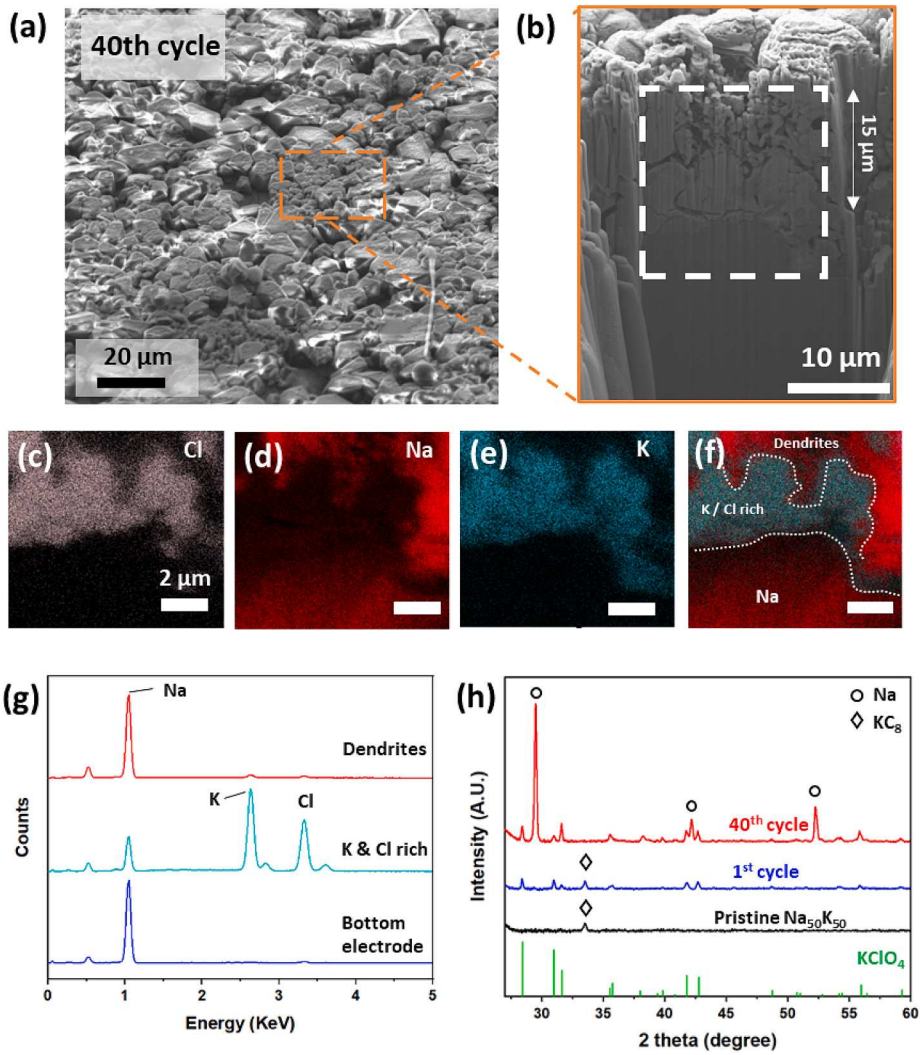

Fig. 4. Cryo-FIB/SEM images and XRD from the $Na_{50}K_{50}$ electrode after 40 cycles. (a) Top surface of the liquid metal after 40 cycles. (b-f) Cross-section milled by cryo-FIB and associated EDS elemental maps show that $KClO_4$ predominately forms on the electrode surface. (g) The composition of dendrite deposition and of the bottom electrode was identified by their corresponding EDS spectra. (h) XRD measurements of the pristine electrode, and electrodes after the first and 40th cycle.

further below (Fig. 4h). Fig. 3g–l presents the embedded cross-section after cryo-milling and EDS maps from the white boxed region of the cross-section. The EDS map for Na and K shows that the electrode is still rich in Na and K, with an atomic ratio of 48:52, suggesting the liquid phase is maintained during the first cycle (Figure S3).

The detection of $KClO_4$ in the electrode after the first cycle suggests the potential dissolution of K from the liquid metal during the cycling process. Interestingly, the dissolved K ions were observed to bind with ClO_4^- anions, precipitating to the electrode surface. This phenomenon is attributed to the limited solubility of the potassium salt ($KClO_4$) in carbonate solvents, leading to its precipitation as a solid salt once the concentration of $KClO_4$ exceeds the solubility limit (approximately a few hundred times lower than $NaClO_4$ in carbonates) [33–35]. In addition, the Cl map in Fig. 3k indicates exclusive localization of $KClO_4$ at the surface, suggesting the replacement of Na^+ ions in the electrolyte with K^+.

The identification of solid Na dendrites on the liquid $Na_{50}K_{50}$ surface in Fig. 3a is significant, as it explains why there is a gradual increase in the voltage profile of the $Na_{50}K_{50}$ symmetric cell, as discussed earlier for the red curve in in Fig. 2a (more SEM images and EDS maps are available in Figure S4 and S5). During each battery cycle, we believe that Na dendrites are initially stripped from the oxidizing electrode as stripping of dendritic structures typically requires less overpotential as indicated by the second arrow in Fig. 2a. Subsequently, the uniform increase in overpotential (between the second and the third arrow in Fig. 2a) could be partly attributed to K stripping. As K stripping causes composition change in the liquid solution phase, such change will gradually affect the oxidizing potential of K, resulting in the increase in overpotential.

Cryo-FIB/SEM images of the 40th cycle electrode further suggest progressive deposition of $KClO_4$ particles to the surface of the electrode during battery cycles. These images help to explain why the liquid electrode experienced catastrophic failure and showed high over-potentials and impedance after ~ 40th cycle (Fig. 4). The cryo-FIB/SEM image indicates that the top surface of the electrode that had been cycled 40 times was uniformly covered with $KClO_4$ particles, leading to a substantial charging when using a 5 KeV electron beam because of the poor electron conductivity of the salt particles (Fig. 4a). The cross-section formed by cryo-milling in Fig. 4b and associated EDS spectra in Fig. 4c–e revealed that a ≈ 15 μm thick $KClO_4$ layer precipitated on the surface. Additionally, the Na map in Fig. 4d and the combined elemental map in Fig. 4f suggest Na dendrite deposition on the $KClO_4$ layer. This thick layer is an effective electron and ion insulator, and thus blocks Na ion diffusion, thereby accelerating Na dendrite deposition. This confirms that during the battery cycling, K continuously strips to form $KClO_4$ particles, significantly impeding the stable ion and electron transport during the electrochemical reaction. In addition, the merged

EDS mapping and spectrum in Fig. 4f and g suggest that the dominance of K stripping is evident as the electrode beneath the $KClO_4$ particles display only sodium signals, indicating complete transformation into sodium metal. The XRD measurements in Fig. 4h additionally support the formation of $KClO_4$, the dissolution of K, and the emergence of Na metal over battery cycles. Figure S6 includes the raw XRD data from 10 degrees to 60 degrees. We also used X-ray photoelectron spectroscopy (XPS) to confirm $KClO_4$ formation at the electrode surfaces (Fig. 5). The binding energy of K $2p_{3/2}$ spectra before and after 5 cycles shifted from 294 eV to 293.4 eV, which is an indicator of $KClO_4$ formation. Cl 2p spectrum further shows that the binding energy of Cl $2p_{3/2}$, which peaks at 208.7, is ascribed to a bond in ClO_4^- (perchlorate) crystals.

Our theoretical calculations suggest that K dissolution can occur due to the higher reactivity of K in Na_xK_{100-x} alloy, as shown in Figure S2. Consequently, the dissolution of K is expected to occur regardless of the Na_xK_{100-x} composition. To experimentally demonstrate that Na_xK_{100-x} is not a viable high-performance Na-ion anode material, we conducted electrochemical tests on three different Na_xK_{100-x} compositions including $Na_{60}K_{40}$ (liquid phase, x = 60) and $Na_{80}K_{20}$ (a mixture of liquid $Na_{70}K_{30}$ and solid Na phase where x = 20). Fig. 6 displays the cyclability of $Na_{80}K_{20}$, $Na_{60}K_{40}$, $Na_{50}K_{50}$, and Na symmetry cells in 1 M $NaClO_4$ in EC/DMC. We find that the $Na_{80}K_{20}$ cell exhibits similar cyclability to that of the solid Na metal symmetry cell while the performance of the $Na_{60}K_{40}$ cell has experienced a similar overpotential rise as the $Na_{50}K_{50}$ cell after several hundreds of hours. Unlike $Na_{50}K_{50}$, the electrode surfaces were not fully covered with $KClO_4$ as the content (20 %) of $Na_{80}K_{20}$ is much lower than $Na_{50}K_{50}$, resulting in a successful transformation to a pure Na electrode without exhibiting a high overpotential (Figure S7). However, this transformation will make the cells susceptible to dendrite formation, ultimately leading to a short-circuit after approximately 750 h of cycling; the usage of the liquid electrode did not prevent short-circuits at all. Therefore, this experimentally suggests that Na_xK_{100-x} cannot improve the anode performance.

It may be tempting to attribute the failure of the $Na_{50}K_{50}$ cell to the poor solubility of $KClO_4$ instead of K dissolution. It is crucial to note our primary goal: to ascertain whether the $Na_{50}K_{50}$ electrode can function as a Na-ion anode despite of K dissolution. The choice of $NaClO_4$ was intended to observe K dissolution by forming $KClO_4$ during the battery redox reaction, which was observable through the Cryo-FIB/SEM and XRD characterization. In the meantime, as potassium bis (fluoro sulfonyl) imide (KFSI) is well dissolved more than 1 M in carbonate solvents [34], sodium bis (fluoro sulfonyl) imide (NaFSI) was used to explore the effect of salt solubility on the liquid electrode. When 1 M of NaFSI was used as the salt in carbonate electrolytes, dissolution of K was also confirmed by EDS from the cycled electrolytes (Figure S8a). More importantly, the transformation to Na metal from the liquid electrode

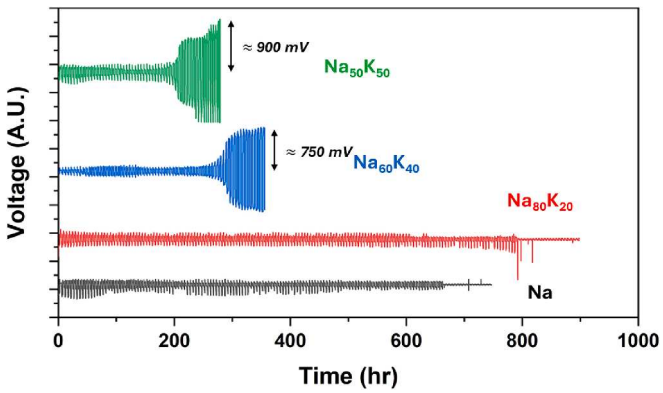

Fig. 6. Cycling performance of $Na_{50}K_{50}$, $Na_{60}K_{40}$, $Na_{80}K_{20}$, and Na symmetric cells. The current density and capacity were 0.4 mA/cm^2 and 1 mAh/cm^2, respectively. The voltage profile from the liquid Na_xK_{100-x} anodes suggests that usage of the liquid anodes did not improve cyclability.

was also confirmed by XRD with the NaFSI electrolyte (Figure S8b). Our results imply that such transformation is universal, regardless of types of Na ion electrolytes, as their thermodynamic potentials are fixed.

One may think that the outcome may change when the liquid Na_xK_{100-x} anodes are cycled in a full cell configuration. We fabricated the two full cells: $Na_{50}K_{50}$ | 1 M $NaPF_6$ – EC – DMC | $Na_{2/3}Ni_{1/3}Mn_{2/3}O_2$ (NNMO) and $Na_{50}K_{50}$ | 1 M $NaClO_4$ – EC – DMC | NNMO. The difference between the $NaClO_4$ and $NaPF_6$ electrolyte is that the solubility of $KClO_4$ is significantly lower than that of KPF_6 so we can compare the effect of their K-salts solubility on the cell performances. Fig. 7a shows the change in the voltage profile of the full cell with the $NaPF_6$ electrolyte at a 1C rate for the first 20 cycles. The first cycle charge profile clearly shows the typical oxidation curve with the two distinct plateaus (around 3.3 V and 3.7 V). Interestingly, after the 5th cycle, the battery voltage profile began to show different plateaus compared to the initial voltage profile. Upon carful comparison of the profile shape with an existing reference [36], the multiple plateaus clearly correspond to the charge/discharge voltage profiles of $K_{2/3}Ni_{1/3}Mn_{2/3}O_2$. The discharge voltage profiles for the first 20 cycles are additionally displayed in Fig. 7b. Furthermore, Fig. 7c presents the cyclic voltammetry (CV) of the cell after the 20 cycles highlighted in red. We also displayed the cyclic voltammetry of the additional two cells ($Na_{50}K_{50}$ | 1 M $NaClO_4$ – EC – DMC | NNMO and Na | 1 M $NaClO_4$ – EC – DMC | NNMO) to compare the transition of the redox pairs with the different anodes and the electrolytes (colored in black and blue). The change in the redox pairs in the cyclic voltammetry clearly indicates that the cathode materials

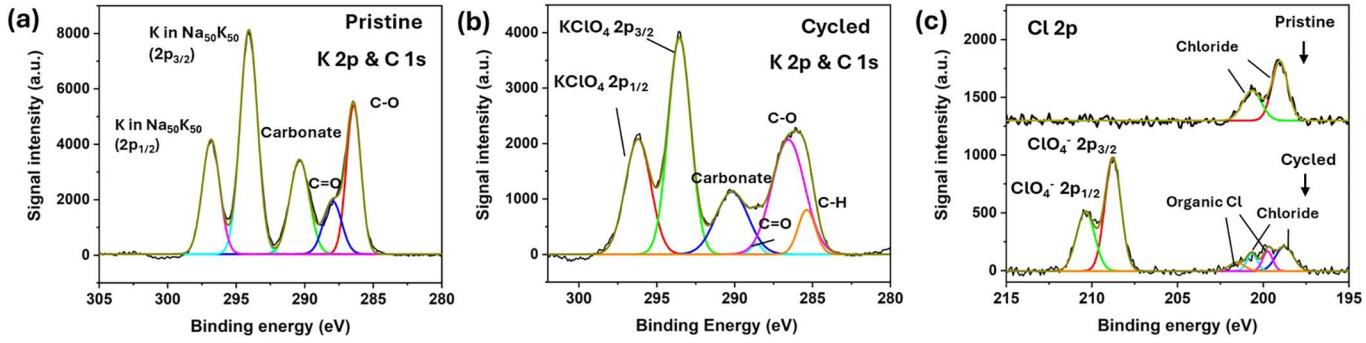

Fig. 5. XPS spectra before and after 5 cycles. (a and b) K 2p and C 1 s spectra of (a) a pristine $Na_{50}K_{50}$ electrode and of (b) the electrode after 5 cycles. (c) Cl 2p spectrum of the pristine electrode and the electrode after 5 cycles. The K $2p_{3/2}$ peak (binding energy at 294 eV) from the pristine alloy appears to be slightly red-shifted compared to pure K metal (294.7 eV) and we believe this is because of the presence of Na-K bonds in the alloy. After the five cycles, the Cl $2p_{3/2}$ peak of the perchlorate signal were observed at 293.4 eV. We found that metal chloride such as NaCl and KCl is present even in the pristine sample possibly due to the impurity of raw Na and K metal chunks during manufacturing. (For interpretation of the references to colour in this figure legend, the reader is referred to the web version of this article.)

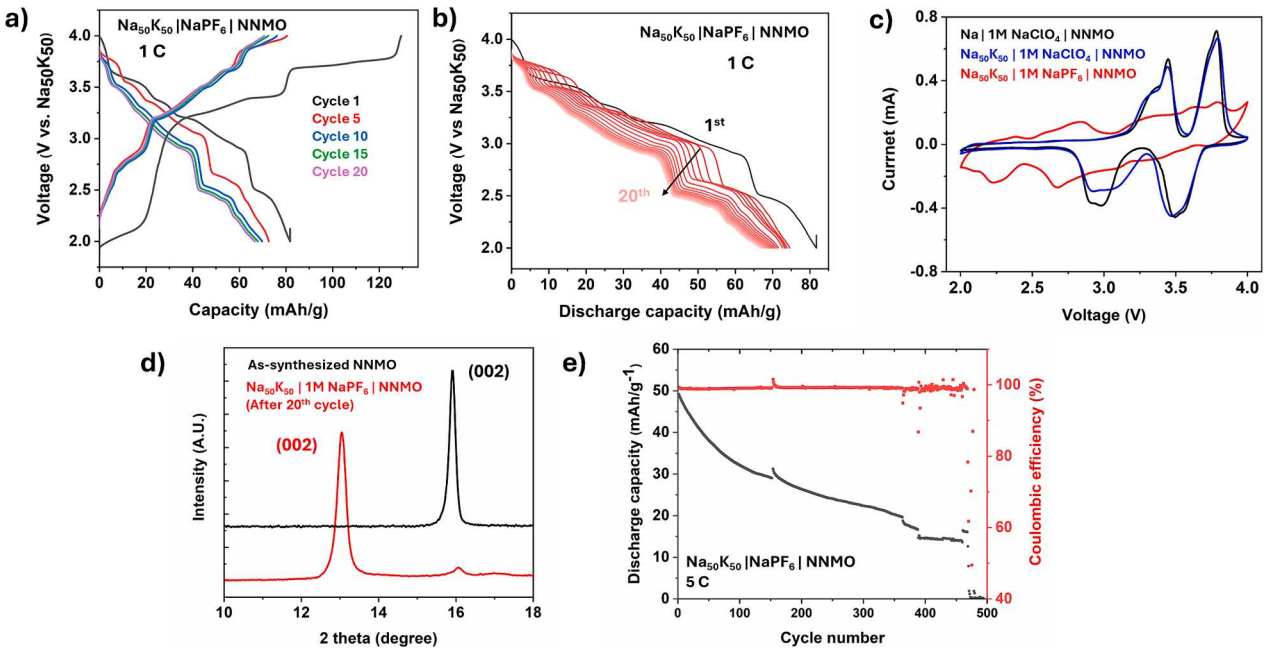

Fig. 7. The electrochemical performance of a full cell in a $NaPF_6$ electrolyte. (a) A voltage profile change in a $Na_{50}K_{50}$ |1 M $NaPF_6$ – EC – DMC | $Na_{2/3}Ni_{1/3}Mn_{2/3}O_2$ (NNMO) cell cycled at a 1C rate. (b) The change in the discharge voltage in the full cell for the first 20 cycles. (c) Cyclic voltammetry of the full cells with a Na anode and a $Na_{50}K_{50}$ anode with a 1 M $NaPF_6$ and $NaClO_4$ electrolyte after 20 cycles. The all curves were captured after 20 cycles (d) XRD of the NNMO cycled in the $Na_{50}K_{50}$ |1 M $NaPF_6$ – EC – DMC | NNMO cell cell after 20 cycles. (e) A performance of the full cell cycled at a 5C rate.

intercalate K^+ ions instead of Na^+ ions in the 1 M $NaPF_6$ electrolyte. After the 20th cycle, ex-situ XRD was performed to reveal changes in d-spacing before and after the use of 1 M $NaPF_6$ (Fig. 7d). After the 20th cycle, the (002) XRD peak position decreased from 15.92° to 13.05°, and the corresponding d-spacing expanded from 0.56 nm to 0.68 nm. Despite the very week diffraction from the K-ions intercalated NNMO at around 16° degrees likely due to the residual unconverted NNMO and potential strain caused by K-ion intercalation, the increase in the (002) layer spacing clearly indicates the large potassium cations intercalated into the layer oxide cathode materials. In addition to XRD, scanning transmission electron microscopy (STEM) additionally identified the presence of K in the NNMO particles cycled in the $NaPF_6$ electrolyte after the 20th cycle (Fig. 8). We believe that this is strong evidence that K continuously dissolves into the liquid electrolyte, transforming the Na-

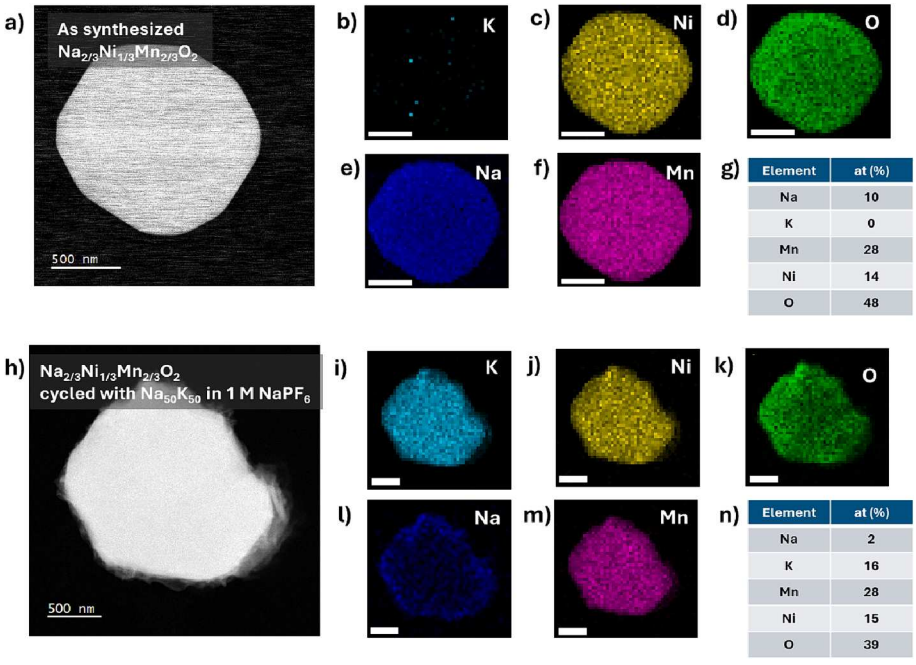

Element	at (%)
Na	10
K	0
Mn	28
Ni	14
O	48

Element	at (%)
Na	2
K	16
Mn	28
Ni	15
O	39

Fig. 8. High-annular angle dark-field scanning electron microscope (HAADF-STEM) images and EDS maps of an as-synthesized NNMO particle and a NNMO particle after 20 cycles. (a) A HAADF-STEM image of the as-synthesized NNMO particle. (b-f) The elemental maps of K, Ni, O, Na, and Mn from the particle. (g) An overall elemental composition table of the particle. (h) A HAADF-STEM image of the NNMO particle after 20 cycles in the $NaPF_6$ electrolyte. (b-f) The elemental maps of K, Ni, O, Na, and Mn from the potassiated particle and (n) its overall elemental composition table. Scale bars in b-f and i-m is 500 nm.

ion battery to a K-ion battery. Such transformation is not always ideal as diffusion of K-intercalation in the layered oxide materials becomes sluggish due to its larger size, leading to a low battery performance at a fast-charging rate (such as 5C) as displayed in Fig. 7e.

To make use of liquid Na_xK_{100-x} as a Na-ion anode, one may use $NaClO_4$ electrolytes, considering its counter K-salt does not dissolves well in battery solvents. We, indeed, confirmed that the full cell with the $NaClO_4$ electrolyte still functions as a Na-ion battery as the CV curves did not change after cycles (Fig. 7c). However, high mass loading or areal capacity of the electrode is inevitably required to compensate for dissolution of K. Nevertheless, the asymmetric reaction during charge and discharge significantly depletes Na ions in the electrolyte while adding more K salts to the electrode surfaces. When used in a full cell configuration, this will eventually create high overpotentials because of lower Na concentrations. Consequently, although some of $Na_{50}K_{50}$ anodes appear to cycle well in the beginning, the fate of the liquid metal in Na-ion anodes will be twofold: (1) precipitation of K salts to an extent that the system becomes solid, which facilitates dendrite deposition and (2) a high overpotential due to lack of Na-ion concentrations in battery electrolytes or to sluggish K-ion intercalation into Na-cathode materials.

To further examine the effect of the anode mass loading on the electrochemical performance of the full cell configuration, we synthesized $Na_{50}K_{50}$ | $NaClO_4$ - EC - DMC - FEC | NNMO full cells with two different areal mass loading and cycled them at 5C rates (Figure S9). While the capacity of the small area mass loading (9.9 mg/cm^2) decayed rapidly after around the 150th cycles, the cell with the large mass loading (27 mg/cm^2) exhibited a gradual decline in capacity and eventually ceased to generate any capacity after approximately the 1000th cycles. The cell with the small mass loading is prone to premature phase transformation into a solid Na metal in early cycles, which makes the cell vulnerable to unstable electron and charge transport caused by $KClO_4$ passivation. On the other hand, we attribute the gradual decay in the capacity from the cell with the large mass loading not only to the $KClO_4$ deposition but also to the continuous decrease in Na ions in the electrolyte due to the replacement between Na and K ions. Consequently, our data suggests that even with excess $Na_{50}K_{50}$ mass loading to slow down the phase transformation, the $Na_{50}K_{50}$ metal anode cannot sustainably function for Na-ion batteries. Furthermore, we demonstrate that excessive anode mass loading of $Na_{50}K_{50}$ compared to the capacity of cathode (often termed as N/P ratio [37]) may have led to a misleading augmented battery performance of the liquid metal in literature.

3. Conclusions

In conclusion, we have examined the feasibility of $Na_{50}K_{50}$ alloy in Na-ion electrolytes using an electrolyte of $NaClO_4$ in carbonates by fabricating $Na_{50}K_{50}$ symmetric cells. By using cryogenic focused ion beam/scanning electron microscope and ex-situ X-ray diffraction, we found that K metal in the alloy gradually dissolves over cycles with the dissolved ions binding with anions (ClO_4^-) to form a solid $KClO_4$ insulating layer. This layer introduces significant impedance to electron and ion transport, which was demonstrated by electrochemical impedance spectroscopy (EIS). Furthermore, the progressive depletion of K in the alloy finally transforms the liquid composition into solid Na metal. This loss of K in the liquid electrode is universal regardless of salt solubility. Therefore, our finding strongly suggests that the Na_xK_{100-x} alloy cannot function as a sustainable liquid metal anode in Na-ion electrolytes without fundamentally altering the system to change the thermodynamic potentials.

CRediT authorship contribution statement

Hyeongjun Koh: Writing – original draft, Methodology, Investigation, Formal analysis. **Mohamed H. Hassan:** Investigation, Formal analysis. **Stella Lin:** Investigation, Data curation. **Lin Wang:** Methodology. **Eric A. Stach:** Writing – review & editing, Supervision, Resources. **Eric Detsi:** Writing – review & editing, Supervision, Resources, Project administration, Funding acquisition, Conceptualization.

Declaration of competing interest

The authors declare the following financial interests/personal relationships which may be considered as potential competing interests: Eric Detsi reports financial support was provided by U.S. National Science Foundation. Eric Detsi reports a relationship with U.S. National Science Foundation that includes: funding grants. If there are other authors, they declare that they have no known competing financial interests or personal relationships that could have appeared to influence the work reported in this paper.

Data availability

Data will be made available on request.

Acknowledgment

The authors gratefully acknowledge primary financial support from the National Science Foundation (NSF), Division of Materials Research (DMR), Future Manufacturing Research Grant #2134715. This work was carried out in part at the Singh Center for Nanotechnology, which is supported by the NSF National Nanotechnology Coordinated Infrastructure Program under grant NNCI-2025608. Additional support for the Nanoscale Characterization Facility at the Singh Center was provided b the University of Pennsylvania Materials Research Science and Engineering Center (MRSEC) (DMR-1720530; DMR-2309043).

Appendix A. Supplementary data

Supplementary data to this article can be found online at https://doi.org/10.1016/j.cej.2024.151578.

References

[1] L. Xue, H. Gao, W. Zhou, S. Xin, K. Park, Y. Li, J.B. Goodenough, Liquid K-Na alloy anode enables dendrite-free potassium batteries, Adv. Mater. 28 (2016) 9608–9612, https://doi.org/10.1002/adma.201602633.
[2] Y. Ding, X. Guo, Y. Qian, H. Gao, D.H. Weber, L. Zhang, J.B. Goodenough, G. Yu, In situ formation of liquid metals via galvanic replacement reaction to build dendrite-free alkali-metal-ion batteries, Angew. Chem. Int. Ed. 59 (2020) 12170–12177, https://doi.org/10.1002/anie.202005009.
[3] Y. Ding, X. Guo, Y. Qian, L. Zhang, L. Xue, J.B. Goodenough, G. Yu, A liquid-metal-enabled versatile organic alkali-ion battery, Adv. Mater. 31 (2019) 1806956, https://doi.org/10.1002/adma.201806956.
[4] D. Yu, X. Guo, G. Yu, Next-generation liquid metal batteries based on the chemistry of fusible alloys, ACS Central Science 6 (2022) 1355–1366, https://doi.org/10.1021/acscentsci.0c00749.
[5] X. Wu, W. Zhang, N. Wu, S.-S. Pang, Y. Ding, G. He, Structural evolution upon delithiation/lithiation in prelithiated foil anodes: a case study of agli alloys with high li utilization and marginal volume variation, Adv. Energy Mater. 11 (2021) 2003082, https://doi.org/10.1002/aenm.202003082.
[6] Q. Sang, S. Hao, J. Han, Y. Ding, Dealloyed nanoporous materials for electrochemical energy conversion and storage, EnergyChem 4 (2022) 100069, https://doi.org/10.1016/j.enchem.2022.100069.
[7] M.M. Butala, V.V.T. Doan-Nguyen, A.J. Lehner, C. Göbel, M.A. Lumley, S. Arnon, K.M. Wiaderek, O.J. Borkiewicz, K.W. Chapman, P.J. Chupas, M. Balasubramanian, R. Seshadri, Operando studies reveal structural evolution with electrochemical cycling in Li–CoS2, J. Phys. Chem. C 122 (2018) 24559–24569, https://doi.org/10.1021/acs.jpcc.8b07828.
[8] L. Wang, S.S. Welborn, H. Kumar, M. Li, Z. Wang, V.B. Shenoy, E. Detsi, High-rate and long cycle-life alloy-type magnesium-ion battery anode enabled through (de) magnesiation-induced near-room-temperature solid-liquid phase transformation, Adv. Energy Mater. 9 (2019) 1902086, https://doi.org/10.1002/aenm.201902086.
[9] K. Hojong, D.A. Boysen, J.M. Newhouse, S. Brian L., C. Brice, B. Paul J., B. David J., J. Kai, T. Alina A., K. Wang, W. Wei, L.A. Ortiz, S.A. Barriga, S.M. Poizeau, D.R. Sadoway, Liquid Metal Batteries: Past, Present, and Future, Chemical Reviews 113 (2013) 2075–2099.

[10] L. Wang, J. Nelson Weker, R. Family, J. Liu, E. Detsi, Morphology evolution in self-healing liquid-gallium-based mg-ion battery anode, ACS Energy Lett. 8 (2023) 4932–4940, https://doi.org/10.1021/acsenergylett.3c01761.
[11] W. Yuan, Y. Li, T. Ding, L. Zhang, J. Shu, Dendrite-free NaK alloy Anodes: electrodes preparation and interfacial reaction, Chem. Eng. J. 432 (2022) 134353, https://doi.org/10.1016/j.cej.2021.134353.
[12] J. Cui, B. Jin, A. Xu, J. Li, M. Shao, Single-Atom Metallophilic Sites for Liquid NaK Alloy Confinement toward Stable Alkali-Metal Anodes, Adv. Sci. 10 (2023) 2206479, https://doi.org/10.1002/advs.202206479.
[13] J. Yang, X. Wang, S. Huang, X. Zhang, J. Chen, Room-temperature fabrication of a liquid NaK alloy-based membrane electrode for sodium-ion batteries, ACS Appl. Mater. Interfaces 12 (2020) 20423–20428, https://doi.org/10.1021/acsami.0c01957.
[14] L. Zhang, S. Peng, Y. Ding, X. Guo, Y. Qian, H. Celio, G. He, G. Yu, A graphite intercalation compound associated with liquid Na–K towards ultra-stable and high-capacity alkali metal anodes, Energy Environ. Sci. 12 (2019) 1989–1998, https://doi.org/10.1039/C9EE00437H.
[15] Q. Ni, Y. Xiong, Z. Sun, C. Sun, Y. Li, X. Yuan, H. Jin, Y. Zhao, Rechargeable sodium solid-state battery enabled by in situ formed Na–K interphase, Adv. Energy Mater. 13 (2023) 2300271, https://doi.org/10.1002/aenm.202300271.
[16] Y. Cheng, M. Li, X. Yang, X. Lu, D. Wu, Q. Zhang, Y. Zhu, M. Gu, Na–K alloy anode for high-performance solid-state sodium metal batteries, Nano Lett. 22 (2022) 9614–9620, https://doi.org/10.1021/acs.nanolett.2c03718.
[17] X. Guo, Y. Liu, X. Zhang, Z. Ju, Y. Li, D. Mitlin, G. Yu, Revealing the solid-state electrolyte interfacial stability model with Na–K liquid alloy, Angew. Chem. Int. Ed. 61 (2022) e202203409, https://doi.org/10.1002/anie.202203409.
[18] X. Guo, J. Bae, Y. Ding, X. Zhang, G. Yu, Liquid alloy enabled solid-state batteries for conformal electrode-electrolyte interfaces, Adv. Funct. Mater. 31 (2021) 2010863, https://doi.org/10.1002/adfm.202010863.
[19] J. Suo, Q. Zhao, H. Tian, L. Wang, L. Dai, J. Luo, S. Liu, Designing a quasi-liquid alloy interface for solid na-ion battery, ACS Nano 17 (2023) 10229–10235, https://doi.org/10.1021/acsnano.3c00397.
[20] L. Wang, Y. Lu, J. Liu, M. Xu, J. Cheng, D. Zhang, J.B. Goodenough, A Superior low-cost cathode for a na-ion battery, Angew. Chem. Int. Ed. 52 (2013) 1964–1967, https://doi.org/10.1002/anie.201206854.
[21] J. Song, L. Wang, Y. Lu, J. Liu, B. Guo, P. Xiao, J.-J. Lee, X.-Q. Yang, G. Henkelman, J.B. Goodenough, Removal of interstitial H2O in hexacyanometallates for a superior cathode of a sodium-ion battery, J. Am. Chem. Soc. 137 (2015) 2658–2664, https://doi.org/10.1021/ja512383b.
[22] J. Zhang, W. Wang, W. Wang, S. Wang, B. Li, Comprehensive review of P2-Type Na2/3Ni1/3Mn2/3O2, a potential cathode for practical application of na-ion batteries, ACS Appl. Mater. Interfaces 11 (2019) 22051–22066, https://doi.org/10.1021/acsami.9b03937.
[23] C.W. Bale, P. Chartrand, S.A. Degterov, G. Eriksson, K. Hack, R. Ben Mahfoud, J. Melançon, A.D. Pelton, S. Petersen, FactSage thermochemical software and databases, Calphad 26 (2002) 189–228, https://doi.org/10.1016/S0364-5916(02)00035-4.
[24] X. Ren, C. Li, Z. Du, C. Guo, Thermodynamic assessments of six binary systems of alkali metals, Calphad 35 (2011) 446–454, https://doi.org/10.1016/j.calphad.2011.06.005.
[25] L. Xue, H. Gao, Y. Li, J.B. Goodenough, Cathode dependence of liquid-alloy Na–K anodes, J. Am. Chem. Soc. 140 (2018) 3292–3298, https://doi.org/10.1021/jacs.7b12267.
[26] Y. Li, H. Wang, W. Yuan, Y. Luo, J. Tu, L. Zhang, J. Shu, Ion competition and limiting dendrite growth models of hybrid-ion symmetric cell, Energy Storage Mater. 42 (2021) 268–276, https://doi.org/10.1016/j.ensm.2021.07.035.
[27] T. Ding, Y. Chen, W. Yuan, L. Li, P. Mou, Y. Luo, H. Yu, L. Yan, J. Shu, L. Zhang, Suitability of NaK alloy for the sodium or potassium metal batteries: Competition between cathode size effect and ion reaction priority effect, Chem. Eng. J. 475 (2023) 146185, https://doi.org/10.1016/j.cej.2023.146185.
[28] M.J. Zachman, Z. Tu, L.A. Archer, L.F. Kourkoutis, Nanoscale elemental mapping of intact solid-liquid interfaces and reactive materials in energy devices enabled by cryo-FIB/SEM, ACS Energy Letters 9 (2020), https://doi.org/10.1021/acsenergylett.0c00202.
[29] K.L. Jungjohann, R.N. Gannon, S. Goriparti, S.J. Randolph, L.C. Merrill, D. C. Johnson, K.R. Zavadil, S.J. Harris, K.L. Harrison, Cryogenic laser ablation reveals short-circuit mechanism in lithium metal batteries, ACS Energy Lett. 6 (2021) 2138–2144, https://doi.org/10.1021/acsenergylett.1c00509.
[30] F.N. Rhines, Phase diagrams in metallurgy : their development and application, McGraw-Hill, 1956. https://cir.nii.ac.jp/crid/1130282270609587840.
[31] K.N. Wood, M. Noked, N.P. Dasgupta, Lithium metal anodes: toward an improved understanding of coupled morphological, Electrochemical, and Mechanical Behavior, ACS Energy Lett. 2 (2017) 664–672, https://doi.org/10.1021/acsenergylett.6b00650.
[32] B.-A. Mei, J. Lau, T. Lin, S.H. Tolbert, B.S. Dunn, L. Pilon, Physical interpretations of electrochemical impedance spectroscopy of REDOX ACtive electrodes for electrical energy storage, J. Phys. Chem. C 122 (2018) 24499–24511, https://doi.org/10.1021/acs.jpcc.8b05241.
[33] L. Hnedkovsky, G. Hefter, Densities and apparent molar volumes of aqueous solutions of NaClO4, KClO4, and KCl at temperatures from 293 to 343 K, J. Chem. Eng. Data 66 (2021) 3645–3658, https://doi.org/10.1021/acs.jced.1c00495.
[34] T. Hosaka, K. Kubota, H. Kojima, S. Komaba, Highly concentrated electrolyte solutions for 4 V class potassium-ion batteries, Chem. Commun. 54 (2018) 8387–8390, https://doi.org/10.1039/C8CC04433C.
[35] N. Peruzzi, B.W. Ninham, P. Lo Nostro, P. Baglioni, Hofmeister phenomena in nonaqueous media: the solubility of electrolytes in ethylene carbonate, J. Phys. Chem. B 116 (2012) 14398–14405, https://doi.org/10.1021/jp309157x.
[36] M.G.T. Nathan, N. Naveen, W.B. Park, K.-S. Sohn, M. Pyo, Fast chargeable P2–K~2/3[Ni1/3Mn2/3]O2 for potassium ion battery cathodes, J. Power Sources 438 (2019) 226992, https://doi.org/10.1016/j.jpowsour.2019.226992.
[37] K.B. Hatzell, Anode-less or anode-free? ACS Energy Lett. 8 (2023) 4775–4776, https://doi.org/10.1021/acsenergylett.3c02163.